Catalysis Today 284 (2017) 52–58

Contents lists available at ScienceDirect

Catalysis Today

journal homepage: www.elsevier.com/locate/cattod

Cyan titania nanowires: Spectroscopic study of the origin of the self-doping enhanced photocatalytic activity

Péter Szirmai[a,*], Bálint Náfrádi[a,*], Alla Arakcheeva[a,b], Edit Szilágyi[c], Richárd Gaál[a], Norbert M. Nemes[d], Xavier Berdat[a], Massimo Spina[a], Laurent Bernard[a], Jaćim Jaćimović[a,e], Arnaud Magrez[a], László Forró[a], Endre Horváth[a,*]

[a] Laboratory of Physics of Complex Matter, Ecole Polytechnique Fédérale de Lausanne, Station 3, CH-1015 Lausanne, Switzerland
[b] Phase Solutions Co Ltd, CH-1012 Lausanne, Chemin des Mésanges 7, Switzerland
[c] Institute for Particle and Nuclear Physics, Wigner Research Centre for Physics, Hungarian Academy of Sciences, Konkoly-Thege Miklós út 29-33, 1121 Budapest, Hungary
[d] Universidad Complutense de Madrid, GFMC, Dpto. Física Aplicada III, Facultad de Ciencias Físicas, CEI Moncloa, 28040 Madrid, Spain
[e] ABB Switzerland, Corporate Research Center, Segelhofstrasse 1 K, Baden Daettwill, Switzerland

ARTICLE INFO

Article history:
Received 26 May 2016
Received in revised form
28 September 2016
Accepted 23 October 2016
Available online 28 October 2016

Keywords:
Titania nanowires
Ti^{3+} surface centers
EPR

ABSTRACT

We report a detailed spectroscopic study of Ti^{3+} self-doped TiO_2 nanowires prepared by high temperature annealing of the protonated titanate nanowires (TiONW) in hydrogen atmosphere. Hydrogenation causes a color change from white to cyan and a major increase of photocatalytic activity. Combination of synchrotron X-ray diffraction and Rutherford backscattering spectrometry revealed that the bulk of the protonated titanate and Ti^{3+} self-doped titania is identical. Raman spectroscopy combined with local laser heating indicated the presence of optically active states in the hydrogenated TiO_2 nanowires. Using multi-frequency electron paramagnetic resonance spectroscopy (EPR), the presence of Ti^{3+} surface states on the cyan titania nanowires is confirmed. We argue that these surface point defects are responsible for enhanced visible light absorption and improved their photocatalytic performance.

1. Introduction

Since the discovery that titanium dioxide (TiO_2) can be applied as a catalyst for water-splitting, over 100 photocatalysts have been found [1]. Amongst these materials, the most intensive research interest is related to titanium dioxide due to its stability in a broad range of chemical environments and its environmental friendliness. The applications of photocatalysis vary from environmental cleanup and clean H_2 energy production to solar cells [2–5]. In the photoactivation mechanism, photogenerated carriers are formed upon the absorption of light. In the valence band, the photogenerated holes migrate to the surface and react with adsorbed water, leaving hydroxyl radicals (OH^-) behind, and oxidizing nearby organic molecules. Photogenerated electrons react with molecular oxygen to produce superoxide radical anions (O_2^-). The majority of photogenerated carriers, however, recombine on bulk or surface defects, yielding low photoactivation efficiencies [6].

The efficiency of photocatalytic processes in TiO_2 can be increased either by lowering the large, 3.2 eV bandgap (390 nm), by reducing the recombination of photogenerated electrons and holes, or by using mixed-phase TiO_2. In several studies [7–9], bandgap engineering was achieved by adding dopant ions. The thermal instability and the increased number of recombination centers in these materials, however, pose difficulties for this method. Self-doped, pure TiO_2 might overcome these limitations. Tao *et al.* [10] synthesized a new surface phase with 2.1 eV bandgap in rutile TiO_2. High-pressure hydrogenation resulted in black TiO_2 nanoparticles with only 1.0 eV bandgap [11].

Degussa P25, which became a standard material in the field of photocatalytic reactions, contains anatase and rutile nanoparticles [12]. The intimate contact of the two phases is believed to be at the origin of its efficiency. The lower bandgap of rutile helps to improve light harvesting efficiency, and closeness of wider bandgap anatase helps separate photoexcited electron-hole pairs, giving them time to do redox chemistry [13]. The photocatalytic activity of Degussa P25, however, might be overcome by the long one-dimensional titania nanowires possessing larger specific surface area depending on the synthesis process and the annealing methods [14].

* Corresponding authors.
E-mail addresses: peter.szirmai@epfl.ch (P. Szirmai), balint.nafradi@epfl.ch (B. Náfrádi), endre.horvath@epfl.ch (E. Horváth).

http://dx.doi.org/10.1016/j.cattod.2016.10.024
0920-5861/

Alternatively, the engineering of the number of surface and bulk defects can decrease the recombination, leading to better photocatalytic properties. The relevance of the defects has been shown both theoretically [15] and experimentally by scanning tunneling microscopy and electron paramagnetic resonance (EPR) [16,17]. In a positron annihilation study, Kong *et al.* [18] pioneered the investigation of the effect of the surface to bulk defect ratio. Decreasing the relative concentration of the bulk defects to the number of surface defects significantly improves the electron-hole separation, thus significantly enhances the photocatalytic efficiency. Several methods have been developed to increase the Ti^{3+} surface state concentration and to control the dimensionality of TiO_2: thin films with strong oxygen sub-stoichiometry [19], rutile TiO_2 nanocrystals with desired facets [20], and one-dimensional titanium dioxide architectures [21] were found to result in increased photoactivity. More recently, two-photon photoemission spectroscopy studies combined with density-functional theory calculations revealed that the Jahn-Teller induced splitting of the 3*d* orbitals of Ti^{3+} is responsible for the enhancement of the photoactivity [22].

Herein, we compare the structure and photocatalytic activity of the hydrogen- and oxygen-annealed protonated titania nanowires. We observed that the hydrogenation of the $H_2Ti_3O_7$ results in better titania photocatalytic activity. Detailed synchrotron X-ray diffraction (XRD) and Rutherford backscattering spectrometry (RBS) measurements of the cyan and white titania do not find any difference in their bulk structure. The EPR spectrum of the cyan colored hydrogenated titanium dioxide nanowires is dramatically different from that of white colored titanium dioxide nanowires. The new EPR line that emerges in H:TiO_2NW is assigned to Ti^{3+} surface states.

2. Experimental methods

Protonated titanate ($H_2Ti_3O_7$) nanowires were prepared by a two-step hydrothermal process. The details about the typical synthesis procedure are given elsewhere [5]. The white powder of layered protonated titanate nanowires (TiONW) is heat treated in H_2 flow at 600 °C for 1 h. The cyan colored hydrogenated titanium oxide nanowire (H:TiO_2NW) product was cooled fast to room temperature. Heat treatment of cyan H:TiO_2NW in air at 350 °C for 30 min resulted in white TiO_2NW. The color change from cyan to white is instantaneous upon heat treatment. Thermogravimetric analysis (TGA) of H:TiO_2NW showed that the color change is followed by oxygen uptake at ~250 °C (see Supporting information).

The same samples can be transformed between TiO_2NW and H:TiO_2NW forms reversibly allowing the study of the same sample in both forms. The specific surface area of H:TiO_2NW, TiO_2NW, and Degussa P25 is measured by the BET method [5], and found to be 60 m^2/g, 60 m^2/g, and 50 m^2/g, respectively.

Scanning electron microscope (SEM) images were taken with a MERLIN Zeiss electron microscope.

To measure electrical resistivity an assembly of nanowires was pressed to form a pellet. The samples were contacted by silver paste and gold wires. Four-point resistivity measurements were realized by using Measuring Unit Keithley 236 that is capable to measure highly resistive samples. The measurements were done independently in two operating modes: *i)* applying current and measuring potential difference between two ends of the sample and *ii)* applying voltage and measuring the electrical current through the sample. Within the experimental error the same results were obtained.

Photocatalytic properties of the commercial Degussa P25, the TiO_2NW and the H:TiO_2NW samples were examined by the measurement of the decomposition rate of methyl orange in the presence of the photocatalysts. The samples (10 mg) were immobilized on porous alumina membranes (47 mm diameter) by suspension making and subsequent filtration [23].

To compare the photocatalytic activity of Degussa P25, the TiO_2NW, and the H:TiO_2NW samples, the photocatalysts were placed in the reactor and immersed with 10 ml of 20 mg/l methyl orange water solution. We used an ultraviolet lamp as a light source with a light intensity of 40 mW/cm^2.

To prove the stability of the H:TiO_2NW sample, we performed repetitive photocatalytic degradation tests. The photocatalyst was immersed with 10 ml of 10 mg/l methyl orange water solution. We used a light intensity of 160 mW/cm^2.

Before irradiation, the suspension was constantly stirred for 30 min in the dark to reach equilibrium adsorption of the methyl orange on the samples. After the dark adsorption period, a first sample was taken to determine the initial (C_0) concentration of the dye. The methyl orange concentration was monitored by measuring the change of the maximum absorbance at the wavelength of 508 nm using a UV–vis spectrophotometer (Carry 50 scan) under the illumination of a mercury lamp (Hamamatsu LC5, 365 nm).

XRD was done on powder samples at the Swiss-Norvegian beamline at the wavelength of $\lambda = 0.70135$ Å. The experimental profile has been fitted by the Rietveld refinement of all indicated structures.

Raman measurements were done at 532 nm using a commercial LabRam spectrometer. The spectrometer was operated with a 600 grooves/mm grating. A typical 0.1 mW laser power was used with a built-in microscope (Olympus LMPlan 50/0.50 inf./0/NN26.5), which yields about $2 \times 2\ \mu m^2$ spot. In situ local laser-heating experiments were also performed by increasing the Raman laser power.

The compositions of the samples were characterized by Rutherford Backscattering Spectrometry (RBS) and Elastic Recoil Detection Analysis (ERDA), using the Hungarian Ion-beam Physics Platform accelerator in Budapest. The ion beam of 1620 keV $^4He^+$ obtained from a 5 MeV Van de Graaff accelerator was collimated with 2 sets of four-sector slits to the necessary dimensions of $0.2 \times 1\ mm^2$. The typical ion current was 8 nA as measured by a transmission Faraday cup [24]. To stop the forward scattered $^4He^+$ ions, a Mylar foil of 6 μm thickness was applied before the ERDA detector. The sample analysis always started with ERDA measurements performed simultaneously with RBS at tilt, recoil and scattering angles of 80°, 20°, and 165°, respectively. To determine the hydrogen loss from the samples during the ERDA experiments 20 spectra were recorded with a dose of 0.2 μC. After the ERDA measurements, the RBS experiment was repeated at a 30° tilt with a dose of 20 μC. The sample spectra were simulated with the same layer structure using the RBX program [25].

SQUID measurements were performed on a MPMS-5T magnetometer following the zero-field-cooled/field-cooled (ZFC/FC) magnetization measurements. Magnetization hysteresis loops were measured at $T = 4.2$ K.

EPR measurements were done at several frequencies in the 9.4–420 GHz range. X-band (9.4 GHz) EPR measurements were performed on a commercial Bruker Elexsys E500 spectrometer. Measurements in the 105–420 GHz frequency range were carried out on a home-made quasi optical spectrometer [26,27]. The high sensitivity of the millimeter-wave setup allows detection of ppm concentration of paramagnetic centers [28–31]. The possibility to observe EPR at different frequencies allows the precise determination of microscopic properties of the EPR centers [32–36]. We used Mn:MgO with a known (1.5 ppm) Mn^{2+} concentration as a *g*-factor and intensity standard. The absolute spin-susceptibility was calculated as described elsewhere [37].

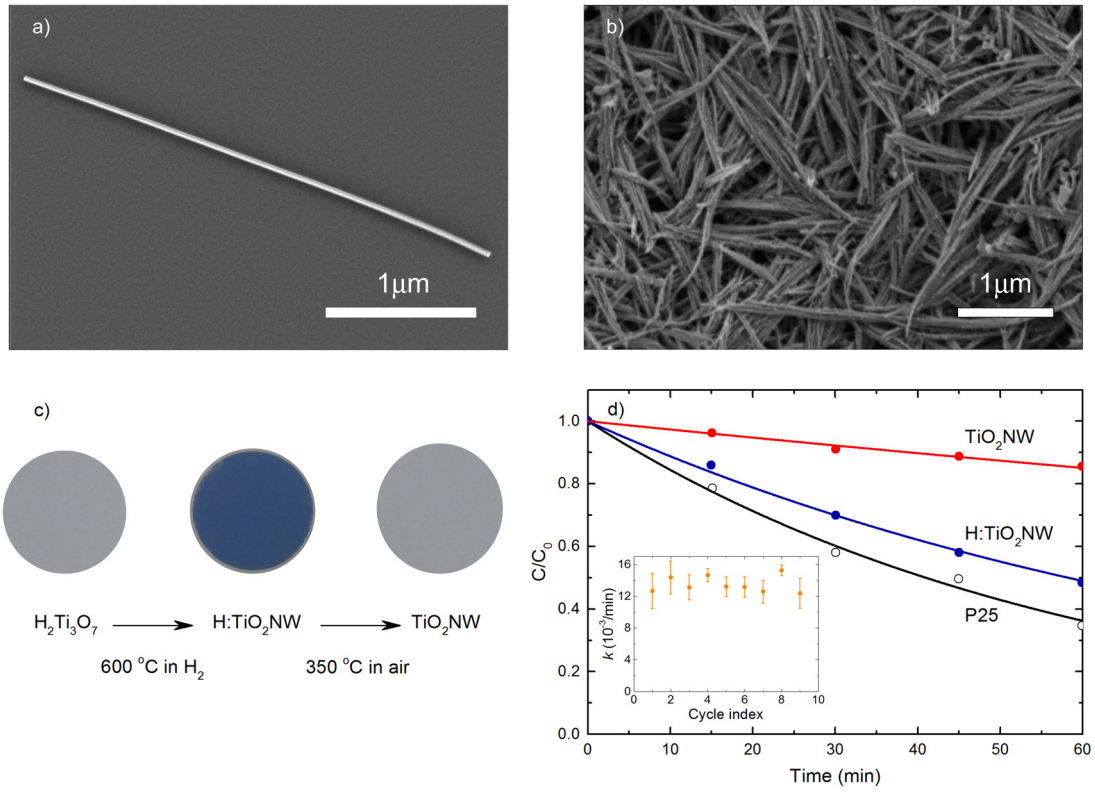

Fig. 1. a) A representative SEM micrograph of an individual titanium oxide nanowire. b) SEM image of the surface of a representative titanium oxide nanowire film immobilized on porous alumina membrane. c) Photographs of TiO_2NW and H:TiO_2NW films immobilized on porous alumina membrane. d) Normalized concentration of methyl orange as a function of irradiation time determined in the presence of Degussa P25, TiO_2 or H:TiO_2NW. Solid lines are exponential fits assuming that the photocatalytic reaction follows first-order reaction kinetics. Inset: Rate constant of H:TiO_2NW calculated from repetitive degradation tests indicating the stability of the surface defects.

3. Results and discussion

White (TiO_2NW) and cyan (H:TiO_2NW) powder samples were prepared (see Fig. 1c) by thermal treatment in hydrogen of $H_2Ti_3O_7$ and calcination of H:TiO_2NW in air, respectively. As can be seen on the SEM micrographs (Fig. 1a and b), both samples were aggregates of nanowires with lengths varying between 1 and 5 μm and with an average diameter of about 60 nm. The photocatalytic properties of TiO_2NW and H:TiO_2NW were measured via the photocatalytic degradation of methyl orange in the presence of the photocatalysts and were compared to that of the Degussa P25 reference. Fig. 1d shows the dependence of C/C_0 on irradiation time. Here, C and C_0 stand for the concentration of methyl orange at a given irradiation time and before irradiation, respectively. We assume that the photocatalytic activity follows first-order reaction kinetics, and the time dependence of C/C_0 can be fitted to a single exponential with a rate constant k ($\ln[C_0/C] = kt$) [38,39]. Comparison of the rate constants of the TiO_2NW ($k = 2.7 \times 10^{-3}$ 1/min), H:TiO_2NW ($k = 1.1 \times 10^{-2}$ 1/min), and Degussa P25 ($k = 1.7 \times 10^{-2}$ 1/min) indicates that hydrogenation leads to a significant increase of the photocatalytic performance, approaching the photoactivity observed for Degussa P25. A similar substantial enhancement of the photocatalytic activity has been found by Chen *et al.* [11] upon hydrogenation of TiO_2 nanocrystals owing to the surface-disorder.

The surface deficiencies in our sample do not change as a function of time and under repetitive photocatalytic degradation tests. As a function of irradiation time, photocatalytic degradation could be satisfactorily fitted with a single exponential rate constant for long irradiation times (see Supporting information) [11]. Furthermore, repetitive photocatalytic degradation tests reveal the unique stability of the surface defects in H:TiO_2NW (see inset of Fig. 1d and Supporting information) [40]. This observation is confirmed by the lack of color change of the H:TiO_2NW film during the degradation tests (see Supporting information).

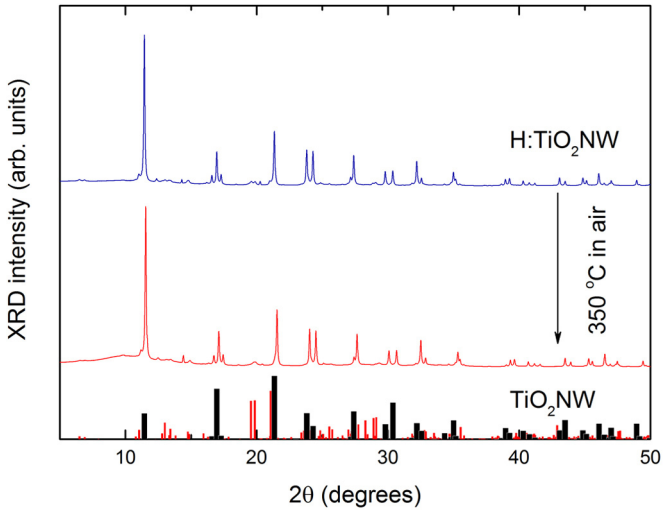

Fig. 2. X-ray diffraction profiles of TiO_2NW and H:TiO_2NW. The spectra are offset for clarity. The broad background is due to the presence of water. Black and red bars indicate the position and intensity of anatase TiO_2 and $Na_{0.18}TiO_2$ structures, respectively. (For interpretation of the references to colour in this figure legend, the reader is referred to the web version of this article.)

Aiming to clarify this significant increase in the photocatalytic activity upon titanate hydrogenation, the structural properties and the presence of defects were characterized using a combination of spectroscopic tools.

Fig. 2 depicts the synchrotron X-ray diffraction (XRD) measurements in H:TiO_2NW and TiO_2NW samples. The TiO_2NW sample was prepared directly from the H:TiO_2NW sample by calcination at 350 °C in air.

Both compounds have predominant anatase TiO_2 (74 wt%) structure [41] (see Supporting information). The detailed analysis of the diffraction profiles shows, however, the presence of other minority components, undetectable in standard laboratory PXRD measurements e.g., $Na_{0.18}TiO_2$ (22 wt%), NaCl (2.4 wt%) and rutile TiO_2 (1.4 wt%). The presence of these secondary phases is due to the incomplete Na to H ion-exchange in layered $Na_2Ti_3O_7$ nanowires [42–44]. These components cannot account for the increased photocatalytic performance of H:TiO_2NW because PXRD showed their presence in both TiO_2NW and in H:TiO_2NW. However, the $Na_{0.18}TiO_2$ might be in close contact with the anatase TiO_2. Similarly to Degussa P25, the mixed phase (anatase and $Na_{0.18}TiO_2$) of the crystallites in our materials might improve the photoactivity of both of our materials.

Analysis of the XRD peak-profiles by the Scherrer equation yields 17 nm as the mean size of the crystallites of TiO_2. This is comparable to the diameter of the individual titanium oxide nanowires (see Fig. 1a) indicating that the bulk of a single nanowire is of perfect structural quality. Similar to the composition, crystallite size is also identical for the H:TiO_2NW and TiO_2NW samples, indicating that the photoactivity and the associated color-change is purely a surface effect. Residual electron density maps, calculated in the vicinity of the oxygen position, evidenced the absence of hydrogen in the bulk of both samples (see Supporting information).

Synchrotron XRD is a powerful tool to identify bulk crystalline minority components, however, surface phases cannot be observed. In order to further characterize the difference between H:TiO_2NW and TiO_2NW samples and set the limit for change in the constituting elements, we performed Rutherford Backscattering Spectrometry (RBS). RBS is sensitive to the mass number of each element, and gives direct information on the depth profiles of the constituents [45,46]. These measurements, in agreement with the XRD studies, find identical chemical composition of H:TiO_2NW and TiO_2NW. RBS revealed that, apart from Ti and O, the major contribution is due to the presence of approximately 2 wt% Na in both samples. As identified by XRD, the Na is present in the form of NaCl and in the form of $Na_{0.18}TiO_2$ in the structure. The Na content is constant as a function of the depth, as confirmed by the RBS depth profile (see Supporting information). This observation completes the XRD study, and supports that the bulk properties of the two samples are identical.

XRD and RBS experiments give direct evidence that the instantaneous color change upon heat treatment in air does not change the bulk crystal structure or composition. Although the surface states might be altered upon heat treatment, this is invisible for XRD and RBS measurements. Raman spectroscopy is a powerful technique to study the molecular environment in the penetration depth of laser light [47]. Complemented with EPR studies, it has proven to give a direct comparison between the surface and the bulk states [48,49]. The tetragonal structure of anatase (with space group D_{4h}^{19} (I_1^4/amd)) results in six Raman-active transitions: three E_g modes centered at approximately 144, 197, and 639 cm^{-1}, two B_{1g} modes at 398 and 519 cm^{-1}, and one mode of A_{1g} symmetry at 514 cm^{-1}, overlapping with the B_{1g} mode at 519 cm^{-1}.

Raman spectra of both TiO_2NW and H:TiO_2NW (see Fig. 3a) recorded at low (0.1 mW) laser power shows the anatase bands [50]. The E_g Raman line around 144 cm^{-1}, which is caused by the symmetric stretching vibration of O-Ti-O, is the most sensitive to the surface defects [51] and to the crystal structure. Fits of the Raman spectra show that the E_g anatase band of H:TiO_2NW and TiO_2NW samples is at 143 cm^{-1} with a linewidth of 10.5 and 9 cm^{-1}, respectively. The observed E_g line characteristics of TiO_2NW are close to the bulk behavior [52,51]. The E_g Raman line, however, is somewhat broader in H:TiO_2NW pointing to the presence of defects in the crystal structure [51] or change in the local coordination [53].

In the Raman experiments described above, low enough (0.1 mW) laser power was chosen to avoid any destruction of the crystal structure. The laser power, however, provides a unique tool to initiate local structural changes of the studied sample [54,55]. Here, we used laser heat treatment to investigate the absorption properties of H:TiO_2NW and TiO_2NW. Raman spectra of H:TiO_2NW after subsequent laser heat treatments are shown in Fig. 3b. At each step, heat treatment is performed with a laser power 10 times higher than in the previous step, and Raman spectra are recorded using the same, 0.1 mW laser power. Upon in-situ heat treatment with the Raman laser (532 nm), H:TiO_2NW turns white locally at the laser focal point. Moreover, the Raman spectrum changes from anatase to a mixture of rutile [56] and anatase.

The Raman spectrum of TiO_2NW, on the other hand, does not change upon a similar laser heat treatment. This points to the presence of color centers on the surface of H:TiO_2NW, in agreement with the absorption spectra (see the Supporting information). The oxygen-deficient surface states in H:TiO_2NW offer a smaller energy barrier for the structural transition. Due to the sample surface absorption, the increasing laser power leads to an increase in local temperature and facilitates the anatase to rutile transformation.

Raman spectroscopy combined with laser heat treatment reveals that the optical activity of the surface states of the hydrogenated titania differs from that of its white counterpart. The origin of the difference was investigated with EPR spectroscopy. The EPR technique provides detailed microscopic information about the oxidation state and the local environment of the paramagnetic ions present in the crystal down to ppm levels [44,57,58,59–61,30,62]. Furthermore, multi-frequency EPR measurements offer a better insight into the interactions, and high-frequency EPR measurements yield more detailed spectroscopic information [63–69].

Fig. 4 shows the EPR spectra of both samples taken at 50 K at 9.4 GHz (a) and at 105 GHz (b). In the TiO_2NW sample, both low- and high-frequency EPR spectra reveal two narrow lines with frequency-independent, paramagnetic g-factor. The two narrow lines at $g_{||} = 1.95$ and $g_{\perp} = 1.99$ correspond to bulk Ti^{3+} states on sites with axial symmetry [70,71] and not to interstitial Ti^{3+} as proposed earlier [72]. The lack of splitting of the EPR lines, even at high-frequency, further supports the strong axial symmetry of the Ti^{3+} site. Hydrogenation dramatically changes the EPR spectra of H:TiO_2NW: in the X-band a broad asymmetric powder line develops with $g_{||} = 1.92$ and $g_{\perp} = 1.94$. The EPR signal broadens with frequency (cf. Fig. 4a and b). The broad powder line in H:TiO_2NW is characteristic to Ti^{3+} ions in a tetragonally distorted octahedral environment [71,72]. Thus we assign it to Ti^{3+} surface paramagnetic defects. The g-value expressions in this case are [71]:

$$g_{||} \cong g_e - 8\lambda/\delta_2$$

$$g_{\perp} \cong g_e - 2\lambda/\delta_1$$

Here g_e is the free-electron g-factor, λ is the spin-orbit coupling, δ_1 and δ_2 are the energy separations of the d-orbitals. Substituting the g-values fitted to the X-band EPR spectra in Fig. 4a ($g_{||} = 1.92$ and $g_{\perp} = 1.94$), and the spin-orbit coupling of Ti^{3+} ($\lambda = 154\ cm^{-1}$) [71] yields $\delta_2 = 15300\ cm^{-1} = 655$ nm (and $\delta_1 = 4900\ cm^{-1} = 2040$ nm). Hence, the material has strong absorption under red light, which agrees with the blue-cyan color seen in Fig. 1.

Low-temperature EPR measurements revealed that the spin-susceptibility of the EPR signals of the surface and bulk Ti^{3+} states do not follow the Curie temperature dependence. The spin-susceptibility decreases more steeply. The EPR signal of the

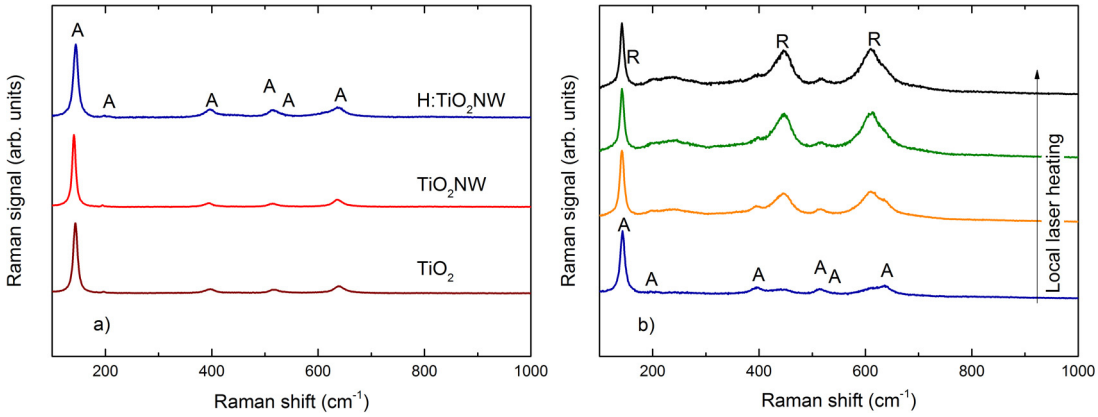

Fig. 3. a) Raman spectra of anatase (TiO_2), TiO_2NW, and H:TiO_2NW at λ = 532 nm. Labels denote the anatase Raman bands. b) Raman spectra of H:TiO_2NW showing the heat treatment influence of increasing laser powers. Note that the local heating in air induces phase transformation from anatase (A) to rutile (R).

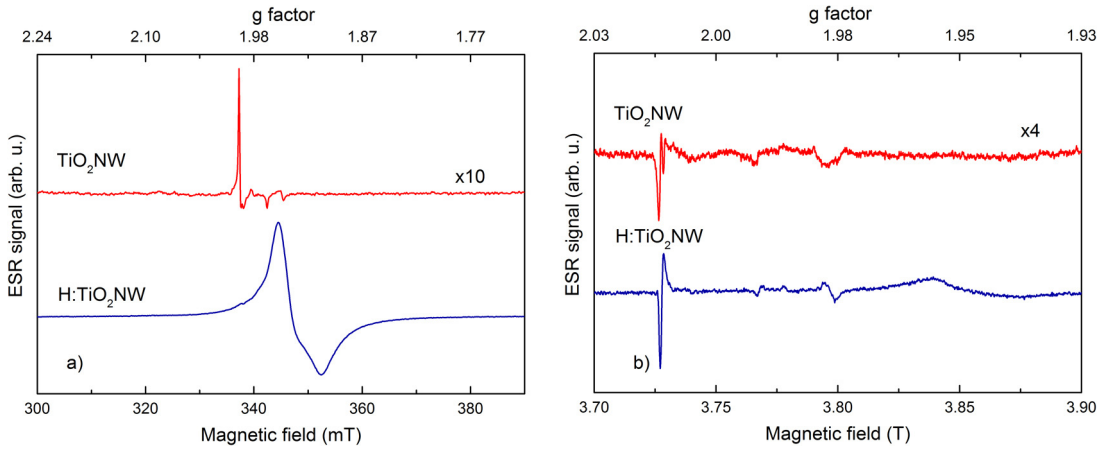

Fig. 4. EPR spectra of H:TiO_2NW and TiO_2NW samples at T = 50 K. a) X-band (9.4 GHz) EPR spectra. The set of EPR lines in H:TiO_2NW around g = 1.94 originates from Ti^{3+} surface states. b) W-band (105 GHz) EPR spectra. Note that the powder EPR line around g = 1.94 broadens with frequency.

surface states almost vanishes above 150 K. We associate the disappearance of the EPR signals at higher temperatures with the recombination of the electron-hole pairs due to diffusion [73,74]. Similarly, Livraghi *et al.* [75] found that the bulk Ti^{3+} state is delocalized over several TiO_6 octahedra at high temperatures. As shown in Ref. [74], these electron traps (Ti^{3+} sites) are due to the nonstoichiometric formation of Ti atoms at the grain boundary.

Due to the drop of the EPR intensity at high temperatures, the absolute magnitude of the spin-susceptibility was determined from the T = 50 K EPR spectra. The spin-susceptibility of the bulk Ti^{3+} states present in both H:TiO_2NW and TiO_2NW is $\chi(Ti^{3+}\ \text{bulk}) = 4.4 \cdot 10^{-11}$ emu/(g·Oe) = $3.8 \cdot 10^{-9}$ emu/(mol·Oe), which corresponds to 4 ppm bulk defect concentration. This indicates a uniquely low oxygen-defect concentration and high material quality. The spin-susceptibility of the broad line at g = 1.94 of H:TiO_2NW is $\chi(Ti^{3+}\ \text{surface}) = 3.88 \cdot 10^{-8}$ emu/(g·Oe) = $3.3 \cdot 10^{-6}$ emu/(mol·Oe). Given that this originates from Ti^{3+} surface states with S = 1/2 spin, this value shows that 1% of the surface Ti ions is in this state. The low value of $\chi(Ti^{3+}\ \text{surface})$ evidences that despite the low amount of defects, the surface states in H:TiO_2NW significantly increase the photocatalytic activity of the material. The increased number of surface defects explains the higher electrical conductivity found in H:TiO_2NW (see Supporting information). As the photocatalytic performance of Degussa P25 was found to be slightly better, we see a further confirmation of the relevance of the unique structure in Degussa P25 with anatase and rutile in close contact.

Through the measurement of the spin-susceptibility, EPR spectroscopy provides direct observation of possible sample degradation, too. It has been suggested in Ref. [76] that due to the surface states the material with a core-shell structure might become unstable at room temperature under ambient conditions. Yet we did not experience any degradation of our H:TiO_2NW sample after 3 years, the amount of surface defects did not decrease.

Earlier reports [77–79] suggest that surface and bulk defects in TiO_2 might induce ferromagnetism. SQUID magnetization measurements (see Supporting information), however, do not show long-range ordering in our materials. The SQUID measurements alone do not provide any information on the origin of the paramagnetic contribution. The paramagnetic temperature dependence and the absolute spin-susceptibility, are in accordance with the Ti^{3+} surface defect states seen by EPR, demonstrating the usefulness of EPR spectroscopy in the study of self-doped TiO_2.

4. Conclusion

Hydrogen-annealed titanium oxide nanowires (TiO_2NWs) show photocatalytic efficiency similar to the industry standard Degussa P25. Surface- and bulk-sensitive measurements were done on both oxygen- and hydrogen-annealed TiO_2 nanowires. X-ray diffraction, RBS and ERDA show that the bulk of the two samples is identical, consisting of ~75 wt% anatase TiO_2, with 22 wt% $Na_{0.18}TiO_2$, NaCl, and rutile TiO_2 as balance. Thermogravimetry indicates oxygen-uptake in hydrogen annealed samples, showing that the surface is

oxygen-deficient. Raman spectroscopy showed that the surface of oxygen-deficient samples could be relatively easily transformed to rutile under intense laser light, while this transition is absent in samples heat-treated in air.

The most striking difference induced by hydrogen annealing has been revealed by multi-frequency EPR. For non-annealed TiO_2NWs, EPR measurements have shown the presence of 4 ppm bulk Ti^{3+}, indicating a uniquely high material quality. Hydrogen-annealed samples have shown Ti^{3+} signals with larger anisotropy, corresponding to surface states. From the *g*-factor anisotropy, we were able to determine the energy separation of the *d*-orbitals giving rise to the EPR signal. This is found to be in the red part of the spectrum, explaining the origin of the cyan color of the samples. This makes the H:TiO_2NWs essentially a core-shell structure, with a shell that absorbs visible light.

The importance of surface states on the photocatalytic activity has already been evoked in Ref. [74]. It has been shown [77] that the proportion of surface and bulk defect states contributes to the photocatalytic activity of TiO_2. In our H:TiO_2NW sample, the surface to bulk defect state ratio is large, thus the high photocatalytic activity is in accordance with the findings of Kong *et al.* [18]. The EPR measurements showed that only 1% of the surface Ti ions are responsible for the notable increase in the photocatalytic activity. Further studies could identify whether increasing the number of surface defect states results in a larger enhancement of the photocatalytic activity.

This study revealed that EPR, as a non-destructive technique, is suitable in the study of the surface to bulk defect ratio and the exact determination of the number of the surface states.

Associated content

Absorption spectra, RBS and ERDA results, SQUID magnetometry, thermogravimetric analysis, and details about synchrotron XRD and transport measurements

Conflict of interest

The authors declare no competing financial interest.

Acknowledgments

Phil Pattison is acknowledged for the synchrotron XRD measurements. The work was supported by the Swiss National Science Foundation (Grant No. 200021_144419) and by grants from Switzerland through the Swiss Contribution (SH/7/2/20). The authors wish to express their deepest and sincerest recognition of Prof. András Dombi a key figure in the topic of photocatalytic materials for the degradation of contaminants of environmental concern.

Appendix A. Supplementary data

Supplementary data associated with this article can be found, in the online version, at http://dx.doi.org/10.1016/j.cattod.2016.10.024.

References

[1] F.E. Osterloh, Chem. Mater. 20 (1) (2008) 35–54.
[2] X. Chen, S.S. Mao, Chem. Rev. 107 (7) (2007) 2891–2959.
[3] K. Nakata, A. Fujishima, J. Photoch. Photobio. C 13 (3) (2012) 169–189.
[4] K. Hashimoto, H. Irie, A. Fujishima, Jpn. J. Appl. Phys. 44 (12R) (2005) 8269.
[5] N. Tétreault, E. Horváth, T. Moehl, J. Brillet, R. Smajda, S. Bungener, N. Cai, P. Wang, S.M. Zakeeruddin, L. Forró, A. Magrez, M. Grätzel, ACS Nano 4 (12) (2010) 7644–7650.
[6] J. Tang, J.R. Durrant, D.R. Klug, J. Am. Chem. Soc. 130 (42) (2008) 13885–13891 (PMID: 18817387).
[7] M.R. Hoffmann, S.T. Martin, W. Choi, D.W. Bahnemann, Chem. Rev. 95 (1) (1995) 69–96.
[8] S.U.M. Khan, M. Al-Shahry, W.B. Ingler, Science 297 (5590) (2002) 2243–2245.
[9] X. Chen, C. Burda, J. Am. Chem. Soc. 130 (15) (2008) 5018–5019.
[10] J. Tao, T. Luttrell, M. Batzill, Nat. Chem. 3 (4) (2011) 296–300.
[11] X. Chen, L. Liu, P.Y. Yu, S.S. Mao, Science 331 (6018) (2011) 746–750.
[12] T. Ohno, K. Sarukawa, K. Tokieda, M. Matsumura, J. Catal. 203 (1) (2001) 82–86.
[13] D.C. Hurum, A.G. Agrios, K.A. Gray, T. Rajh, M.C. Thurnauer, J. Phys. Chem. B 107 (19) (2003) 4545–4549.
[14] H.B. Wu, H.H. Hng, X.W.D. Lou, Adv. Mater. 24 (19) (2012) 2567–2571.
[15] H. Cheng, A. Selloni, Phys. Rev. B 79 (2009) 092101.
[16] Y. He, A. Tilocca, O. Dulub, A. Selloni, U. Diebold, Nat. Mater. 8 (2009) 585–589.
[17] F. Zuo, L. Wang, T. Wu, Z. Zhang, D. Borchardt, P. Feng, J. Am. Chem. Soc. 132 (34) (2010) 11856–11857.
[18] M. Kong, Y. Li, X. Chen, T. Tian, P. Fang, F. Zheng, X. Zhao, J. Am. Chem. Soc. 133 (41) (2011) 16414–16417.
[19] I. Justicia, P. Ordejón, G. Canto, J.L. Mozos, J. Fraxedas, G.A. Battiston, R. Gerbasi, A. Figueras, Adv. Mater. 14 (19) (2002) 1399–1402.
[20] F. Zuo, K. Bozhilov, R.J. Dillon, L. Wang, P. Smith, X. Zhao, C. Bardeen, P. Feng, Angew. Chem. 124 (May (25)) (2012) 6327–6330.
[21] C. Mao, F. Zuo, Y. Hou, X. Bu, P. Feng, Angew. Chem. 126 (39) (2014) 10653–10657.
[22] Z. Wang, B. Wen, Q. Hao, L.-M. Liu, C. Zhou, X. Mao, X. Lang, W.-J. Yin, D. Dai, A. Selloni, et al., J. Am. Chem. Soc. 137 (28) (2015) 9146–9152.
[23] T. Szabó, V. Tóth, E. Horváth, L. Forró, I. Szilágyi, Langmuir 31 (1) (2015) 42–49.
[24] F. Pászti, A. Manuaba, C. Hajdu, A. Melo, M.D. Silva, Nucl. Instrum. Method B 47 (2) (1990) 187–192.
[25] E. Kótai, Nucl. Instrum. Method B 85 (1–4) (1994) 588–596.
[26] B. Náfrádi, R. Gaál, T. Fehér, L. Forró, J. Magn. Reson. 192 (2) (2008) 265–268.
[27] B. Náfrádi, R. Gaál, A. Sienkiewicz, T. Fehér, L. Forró, J. Magn. Reson. 195 (2) (2008) 206–210.
[28] S. Tóth, D. Quintavalle, B. Náfrádi, L. Korecz, L. Forró, F. Simon, Phys. Rev. B 77 (21) (2008).
[29] D.V. Konarev, S.S. Khasanov, A.Y. Kovalevsky, D.V. Lopatin, V.V. Rodaev, G. Saito, B. Náfrádi, L. Forró, R.N. Lyubovskaya, Cryst. Growth Des. 8 (4) (2008) 1161–1172.
[30] F. Simon, M. Galambos, D. Quintavalle, B. Náfrádi, L. Forró, J. Koltai, V. Zólyomi, J. Kürti, N.M. Nemes, M.H. Rümmeli, et al., Phys. Status Solidi B 245 (10) (2008) 1975–1978.
[31] B. Náfrádi, N.M. Nemes, T. Fehér, L. Forró, Y. Kim, J.E. Fischer, D.E. Luzzi, F. Simon, H. Kuzmany, Phys. Status Solidi B 243 (13) (2006) 3106–3110.
[32] A. El-Ghayoury, C. Mézière, S. Simonov, L. Zorina, M. Cobián, E. Canadell, C. Rovira, B. Náfrádi, B. Sipos, L. Forró, et al., Chem. Eur. J 16 (47) (2010) 14051–14059.
[33] K. Nagy, B. Náfrádi, N. Kushch, E. Yagubskii, E. Herdtweck, T. Fehér, L. Kiss, L. Forró, A. Jánossy, Phys. Rev. B 80 (10) (2009).
[34] A. Olariu, B. Náfrádi, L. Ćirić, N.M. Nemes, L. Forró, Phys. Status Solidi B 245 (10) (2008) 2029–2033.
[35] L. Mihály, T. Fehér, B. Dóra, B. Náfrádi, H. Berger, L. Forró, Phys. Rev. B 74 (17) (2006).
[36] F. Simon, H. Kuzmany, B. Náfrádi, T. Fehér, L. Forró, F. Fülöp, A. Jánossy, L. Korecz, A. Rockenbauer, F. Hauke, et al., Phys. Rev. Lett. 97 (13) (2006).
[37] P. Szirmai, G. Fábián, B. Dóra, J. Koltai, V. Zólyomi, J. Kürti, N.M. Nemes, L. Forró, F. Simon, Phys. Status Solidi B 248 (11) (2011) 2688–2691.
[38] J.-M. Wu, M. Antonietti, S. Gross, M. Bauer, B.M. Smarsly, Chem. *Phys. Chem.* 9 (5) (2008) 748–757.
[39] J.-M. Wu, T.-W. Zhang, J. Photochem. Photobiol. A 162 (1) (2004) 171–177.
[40] J.-M. Wu, T.-W. Zhang, Y.-W. Zeng, S. Hayakawa, K. Tsuru, A. Osaka, Langmuir 21 (15) (2005) 6995–7002.
[41] E. Horváth, A. Kukovecz, Z. Kónya, I. Kiricsi, Chem. Mater. 19 (4) (2007) 927–931.
[42] M. Hodos, E. Horváth, H. Haspel, A. Kukovecz, Z. Kónya, I. Kiricsi, Chem. Phys. Lett. 399 (4–6) (2004) 512–515.
[43] M. Hodos, H. Haspel, E. Horváth, Á. Kukovecz, Z. Kónya, I. Kiricsi, AIP Conf. Proc., Vol. 786, AIP Publishing, 2005, pp. 345–348.
[44] J. Jaćimović, E. Horváth, B. Náfrádi, R. Gaál, N. Nikseresht, H. Berger, L. Forró, A. Magrez, Appl. Phys. Lett. Mater. 1 (3) (2013) 1–7.
[45] E. Szilágyi, Nucl. Instrum. Method B 268 (11-12) (2010) 1731–1735.
[46] E. Szilágyi, L. Wielunski, F. Pászti, Nucl. Instrum. Method B 136 (0) (1998) 701–706.
[47] H. Kuzmany, Solid-State Spectroscopy: An Introduction, 2nd edition, Springer, New York, USA, 2009.
[48] P. Szirmai, G. Fábián, J. Koltai, B. Náfrádi, L. Forró, T. Pichler, O.A. Williams, S. Mandal, C. Bäuerle, F. Simon, *2013*, Phys. Rev. B 87 (*2013*) 195132.
[49] P. Szirmai, T. Pichler, O.A. Williams, S. Mandal, C. Bäuerle, F. Simon, Phys. Status Solidi B 249 (12) (2012) 2656–2659.
[50] T. Ohsaka, F. Izumi, Y. Fujiki, J. Raman Spectrosc. 7 (6) (1978) 321–324.
[51] V. Swamy, A. Kuznetsov, L.S. Dubrovinsky, R.A. Caruso, D.G. Shchukin, B.C. Muddle, Phys. Rev. B 71 (2005) 184302.
[52] V. Likodimos, T. Stergiopoulos, P. Falaras, J. Kunze, P. Schmuki, J. Phys. Chem. C 112 (33) (2008) 12687–12696.
[53] B. Choudhury, A,C, Int. Nano Lett. 3 (2013) 1–9.

[54] J.C. Chacón-Torres, A.Y. Ganin, M.J. Rosseinsky, T. Pichler, Phys. Rev. B 86 (2012) 075406.
[55] J.C. Chacón-Torres, A.Y. Ganin, M.J. Rosseinsky, T. Pichler, Phys. Status Solidi B 249 (12) (2012) 2640–2643.
[56] F. Shao, J. Sun, L. Gao, S. Yang, J. Luo, J. Phys. Chem. C 115 (5) (2011) 1819–1823.
[57] P. Szirmai, E. Horváth, B. Náfrádi, Z. Micković, R. Smajda, D.M. Djokić, K. Schenk, L. Forró, A. Magrez, J. Phys. Chem. C 117 (1) (2013) 697–702.
[58] B. Náfrádi, L. Forró, M. Choucair, Phys. Status Solidi B 251 (12) (2014) 2521–2524.
[59] Y. Lakhdar, C. Mézière, L. Zorina, M. Giffard, P. Batail, E. Canadell, P. Auban-Senzier, C. Pasquier, D. Jérome, B. Náfrádi, et al., J. Mater. Chem 21 (5) (2011) 1516.
[60] L. Ćirić, A. Sienkiewicz, B. Náfrádi, M. Mionić, A. Magrez, L. Forró, Phys. Status Solidi B 246 (11–12) (2009) 2558–2561.
[61] L. Ćirić, K. Pierzchala, A. Sienkiewicz, A. Magrez, B. Náfrádi, D. Alexander, J. Warner, H. Shinohara, M.H. Ruemmeli, T. Pichler, et al., Phys. Status Solidi B 245 (10) (2008) 2042–2046.
[62] S. Tóth, D. Quintavalle, B. Náfrádi, L. Forró, L. Korecz, A. Rockenbauer, T. Kálai, K. Hideg, F. Simon, Phys. Status Solidi B 245 (10) (2008) 2034–2037.
[63] Á. Antal, T. Fehér, B. Náfrádi, R. Gaál, L. Forró, A. Jánossy, Physica B 405 (11 Supplement) (2010) S168–S171.
[64] Á. Antal, T. Fehér, E. Tátrai-Szekeres, F. Fülöp, B. Náfrádi, L. Forró, A. Jánossy, Phys. Rev. B 84 (2011) 075124.
[65] B. Náfrádi, Á. Antal, Á. Pásztor, L. Forró, L. Kiss, T. Fehér, E. Kováts, S. Pekker, A. Jánossy, J. Phys. Chem. Lett. 3 (22) (2012) 3291–3296.
[66] B. Náfrádi, M. Choucair, L. Forró, Carbon 74 (2014) 346–351.
[67] B. Náfrádi, M. Choucair, P.D. Southon, C.J. Kepert, L. Forró, Chem. Eur. J. 21 (2) (2014) 770–777.
[68] Á. Antal, T. Fehér, B. Náfrádi, L. Forró, A. Jánossy, Phys. Status Solidi B 249 (5) (2012) 1004–1007.
[69] B. Náfrádi, A. Olariu, L. Forró, C. Mézière, P. Batail, A. Jánossy, Phys. Rev. B 81 (22) (2010).
[70] S. Livraghi, M. Chiesa, M.C. Paganini, E. Giamello, J. Phys. Chem. C 115 (51) (2011) 25413–25421.
[71] M. Chiesa, M.C. Paganini, S. Livraghi, E. Giamello, Phys. Chem. Chem. Phys. 15 (2013) 9435–9447.
[72] R.F. Howe, M. Gratzel, J. Phys. Chem 89 (21) (1985) 4495–4499.
[73] T. Rajh, A.E. Ostafin, O.I. Micic, D.M. Tiede, M.C. Thurnauer, J. Phys. Chem. 100 (11) (1996) 4538–4545.
[74] C.P. Kumar, N.O. Gopal, T.C. Wang, M.-S. Wong, S.C. Ke, J. Phys. Chem. B 110 (11) (2006) 5223–5229.
[75] S. Livraghi, S. Maurelli, M.C. Paganini, M. Chiesa, E. Giamello, Angew. Chem. Int. Ed. 50 (35) (2011) 8038–8040.
[76] A. Naldoni, M. Allieta, S. Santangelo, M. Marelli, F. Fabbri, S. Cappelli, C.L. Bianchi, R. Psaro, V. Dal Santo, J. Am. Chem. Soc. 134 (18) (2012) 7600–7603 (PMID: 22519668).
[77] S. Zhou, E. Cižmar, K. Potzger, M. Krause, G. Talut, M. Helm, J. Fassbender, S.A. Zvyagin, J. Wosnitza, H. Schmidt, Phys. Rev. B 79 (11) (2009).
[78] N.H. Hong, J. Sakai, N. Poirot, V. Brizé, Phys. Rev. B 73 (13) (2006).
[79] S.D. Yoon, Y. Chen, A. Yang, T.L. Goodrich, X. Zuo, D.A. Arena, K. Ziemer, C. Vittoria, V.G. Harris, J. Phys. Condens. Matter 18 (27) (2006) L355–L361.